mater.scichina.com link.springer.com

Published online 12 August 2022 | https://doi.org/10.1007/s40843-022-2144-x
Sci China Mater 2023, 66(1): 257–263

Centrosymmetric to noncentrosymmetric structural transformation in a superconducting high-entropy alloy due to carbon addition

Guorui Xiao[1,2,3], Qinqing Zhu[1,2,4], Wuzhang Yang[1,2,4], Yanwei Cui[1,2,3], Shijie Song[3], Guang-Han Cao[3] and Zhi Ren[1,2*]

ABSTRACT **The tetragonal σ phase is one of the most frequently occurring phases in transition metal alloys. However, the effect of carbon addition in σ type high-entropy alloys (HEAs) has not been studied to date. Here we report the observation of structural transformation by adding carbon in the superconducting $Ta_{10}Mo_5W_{30}Re_{35}Ru_{20}$ HEA (critical temperature T_c = 4.87 K). It is found that the $Ta_{10}Mo_5W_{30}Re_{35}Ru_{20}C_x$ HEA adopts the centrosymmetric σ type structure for $0 \le x \le 2$, but transforms into the noncentrosymmetric β-Mn type structure for $16 \le x \le 20$. The transformed β-Mn type HEA also displays bulk superconductivity with a higher T_c of 5.34 K and an upper critical field approaching the Pauli paramagnetic limit. In addition, the structural transformation is attributed to the decrease in valence electron concentration as well as the increase in lattice distortion and mixing entropy due to carbon addition. Our results not only provide a rare example of centrosymmetric to noncentrosymmetric structural transformation in HEAs, but also consolidate that nonmetallic carbon is an effective additive for tuning the structure and physical properties of HEAs.**

Keywords: high-entropy alloys, structural transformation, carbon adding, superconductivity, noncentrosymmetric

INTRODUCTION

High-entropy alloys (HEAs) have been the subject of intensive studies over the past two decades as an emerging class of multicomponent alloys [1–7]. In contrary to traditional alloys based on one or two elements, HEAs are composed of at least five principled elements whose atomic concentrations vary from 5% to 35%. This large number of constituent elements results in increased mixing entropy, which overcomes the formation enthalpy for intermetallic compounds and leads to the formation of disordered solid solutions. So far, HEAs have been found in various crystal structures, including face-centered-cubic (fcc) [1,2], body-centered-cubic (bcc) [1,2], hexagonal-closed packed (hcp) [1,2], CsCl type [8], α-Mn type [9,10], σ type [11,12] and A15 type [13,14]. Besides their diverse crystal structures, HEAs also display a range of interesting mechanical and physical properties, such as the combination of ductility and high strength [15,16], enhanced corrosion and oxidation resistance [17–20], exceptional thermal stability [21,22], and robust type-II superconductivity [23,24].

Recently, the interaction between HEAs and carbon has attracted increasing attention [25–32]. Given its small atomic radius, carbon prefers to occupy the interstitial position, causing an expansion of the lattice. On one hand, this leads to solid solution strengthening and hence an enhancement in microhardness of HEAs. On the other hand, the lattice expansion may induce a change in the electronic ground state, which allows for a tuning of their physical properties. So far, both these effects have been found in fcc [32] and bcc [31] HEAs. More remarkably, a transformation from the hcp structure to the fcc one is found to occur by adding carbon in the Mo-Re-Ru-Pd-Pt HEAs [32]. In addition, both the hcp and transformed fcc HEAs become superconducting and the key factors that control superconductivity are essentially the same despite their different structures. Given the structural diversity of HEAs, it is of significant interest to see whether a structural transformation can be induced by adding carbon in other structurally different HEAs.

The tetragonal σ phase is one of the most frequently occurring phases in transition metal alloys and of interest from both fundamental and application points of view [33]. As such, considerable efforts have been devoted to establishing the criteria for σ phase formation in HEAs [11,12,34,35]. However, no carbon added σ type HEA has been investigated to date. Here we report the effect of carbon addition on the structure and physical properties of the $Ta_{10}Mo_5W_{30}Re_{35}Ru_{20}$ HEA, which adopts a σ type structure and exhibits bulk superconductivity below 4.87 K. It is found that, upon carbon addition, the $Ta_{10}Mo_5W_{30}Re_{35}Ru_{20}C_x$ HEA transforms into the noncentrosymmetric cubic β-Mn type structure for $16 \le x \le 20$, which also becomes superconducting with an almost x-independent T_c of 5.34 K and an upper critical field around 9.3 T. A comparison is made between the phase stability of σ type and β-Mn type HEAs, and its implication on the origin of structural transformation is discussed.

EXPERIMENTAL SECTION

Ingots of $Ta_{10}Mo_5W_{30}Re_{35}Ru_{20}C_x$ HEAs with $0 \le x \le 25$ were prepared by the standard arc-melting method. Stoichiometric amounts of high-purity Ta (99.9%), Mo (99.9%), W (99.9%), Re

[1] School of Science, Westlake University, Hangzhou 310024, China
[2] Institute of Natural Sciences, Westlake Institute for Advanced Study, Hangzhou 310024, China
[3] Department of Physics, Zhejiang University, Hangzhou 310027, China
[4] Department of Physics, Fudan University, Shanghai 200433, China
* Corresponding author (email: renzhi@westlake.edu.cn)

(99.99%), Ru (99.9%) and C (99.5%) powders were mixed thoroughly and pressed into pellets in an argon filled glove-box. The pellets were then melted four times in an arc furnace, followed by rapid cooling on a water-chilled copper plate. The phase purity of the resulting samples was checked by powder X-ray diffraction (XRD) at room temperature using a Bruker D8 Advance X-ray diffractometer with Cu Kα radiation. The structural refinements were performed using the Lebail method with the JANA2006 programme [36]. The sample morphology, chemical composition and electron backscatter diffraction (EBSD) were investigated on a Zeiss Gemini 450 analytical field emission scanning electron microscope (SEM) equipped with an energy dispersive X-ray (EDX) spectrometer. The microstructure was examined on an FEI Tecnai G2 F20 S-TWIN transmission electron microscope (TEM). Electrical resistivity and specific heat measurements were carried out on a Quantum Design Physical Property Measurement System (PPMS-9 Dynacool). Magnetization measurements were performed on a Quantum Design Magnetic Property Measurement System (MPMS3).

RESULTS AND DISCUSSION

Fig. 1a shows the room-temperature XRD patterns for the series of $Ta_{10}Mo_5W_{30}Re_{35}Ru_{20}C_x$ HEAs with x up to 25, and the data are shown with increasing carbon content x from bottom to top. One can see that the addition of carbon results in a drastic change in the crystal structure and there exist two separated single-phase regions at $0 \le x \le 2$ and $16 \le x \le 20$. In the former region, all the diffraction peaks correspond to the tetragonal σ type structure with the $P4_2/mnm$ space group. The refined lattice parameters are a = 9.6051(3) Å, c = 4.9871(1) Å and a = 9.6064(3) Å, c = 4.9885(1) Å for x = 0 and 2, respectively. It thus seems that the σ phase can accommodate a small amount of carbon, leading to a lattice expansion. In the latter region, however, the number of diffraction peaks is strongly reduced and the pattern is consistent with the cubic β-Mn type structure (space group $P4_132$). Meanwhile, the cubic lattice constant increases monotonically from 6.8181(1) to 6.8308(1) Å, with increasing x from 16 to 20. Between these two regions ($5 \le x \le 12$), the σ and β-Mn type structures are found to coexist, and a small amount of α-Mn type phase is also identified for x = 5. At the highest carbon content of x = 25, fcc and hcp impurity phases start to appear (marked with different symbols) in addition to the main β-Mn type one. Hence the maximum content of carbon that can dissolve in the HEA is x = 20. This is reasonable since, in the β-Mn type structure, the carbon atoms occupy at most one sixth of the total crystallographic sites, which is equivalent of a maximum carbon-to-metal ratio of 20/100. Clearly, a structural transformation is induced by adding carbon in the $Ta_{10}Mo_5W_{30}Re_{35}Ru_{20}$ HEA.

The phase evolution in $Ta_{10}Mo_5W_{30}Re_{35}Ru_{20}C_x$ is confirmed by structural refinements. Representative results for x = 0, 5 and 20 are shown in Fig. 1b–d, and the atomic coordinates used for the refinements are listed in Table 1. In the σ type structure, there are five different crystallographic sites of 2a (0, 0, 0), 4g (0.3986, 0.6014, 0), 8i_1 (0.1312, 0.5365, 0), 8i_2 (0.0661, 0.2607, 0), and 8j (0.3173, 0.3173, 0.2480), and the occupancy of transition metal atoms at each site is fixed according to their stoichiometry.

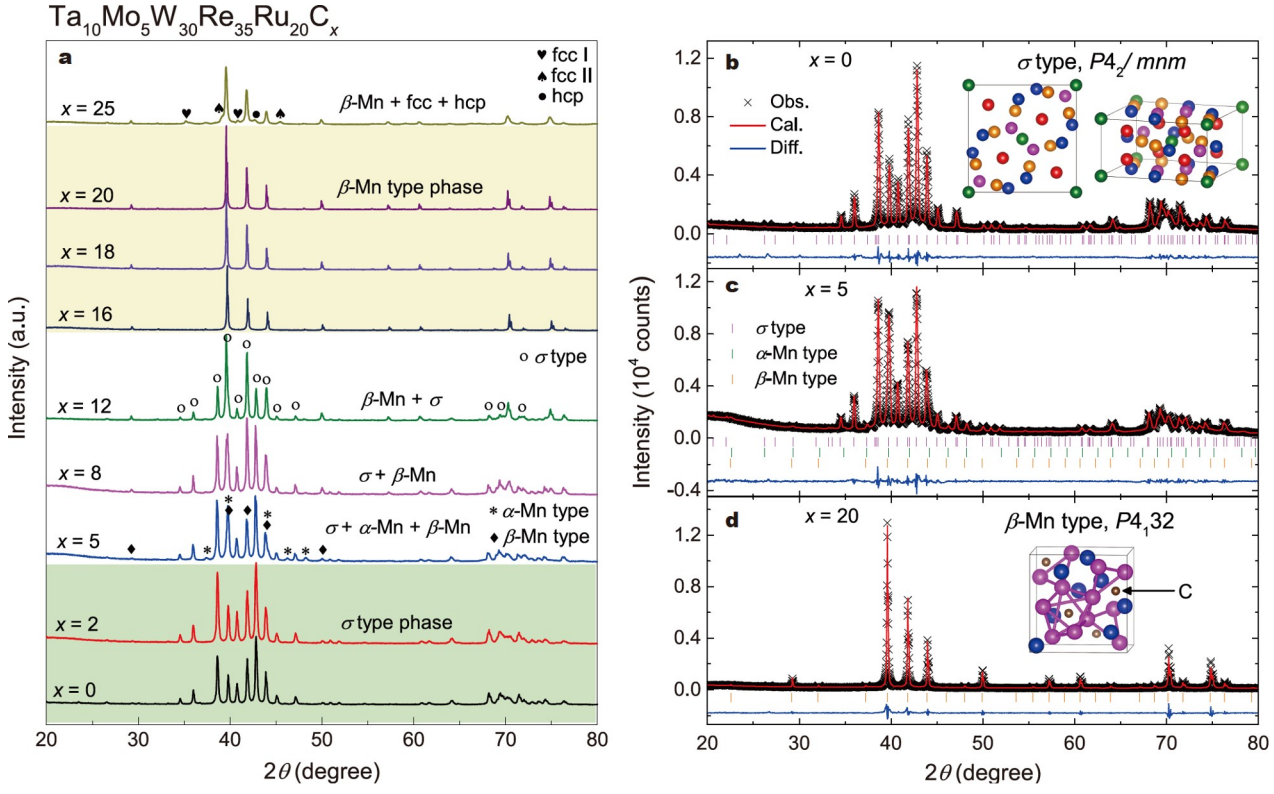

Figure 1 (a) Evolution of room-temperature XRD patterns with carbon content x for the $Ta_{10}Mo_5W_{30}Re_{35}Ru_{20}C_x$ HEAs. The impurity phases for representative samples (x = 5, 12 and 25) are marked with different symbols, respectively. (b–d) The structural refinement profiles for the HEAs with x = 0, 5 and 20, respectively. In panel (b), the insets show the schematic structures of the σ type phase perpendicular and parallel to the c-axis. In panel (d), the inset shows the schematic structure of the β-Mn type phase and the interstitial C atom is marked by the arrow. In both panels, the different crystallographic sites are highlighted in different colors.

Table 1 Atomic coordinates used for the refinements in $Ta_{10}Mo_5W_{30}Re_{35}Ru_{20}C_x$ HEAs (x = 0, 5 and 20). Here M represents the transition metal element.

σ type structure					β-Mn type structure					α-Mn type structure				
atom	site	x	y	z	atom	site	x	y	z	atom	site	x	y	z
M1	2*a*	0	0	0	M1	8*c*	0.0632	0.0632	0.0632	M1	2*a*	0	0	0
M2	4*g*	0.3986	0.6014	0	M2	12*d*	0.125	0.2028	0.4528	M2	8*c*	0.3179	0.3179	0.3179
M3	$8i_1$	0.1312	0.5365	0	C	4*a*	0.375	0.375	0.375	M3	$24g_1$	0.3571	0.3571	0.0346
M4	$8i_2$	0.0661	0.2607	0						M4	$24g_2$	0.0896	0.0896	0.2819
M5	8*j*	0.3173	0.3173	0.2480										

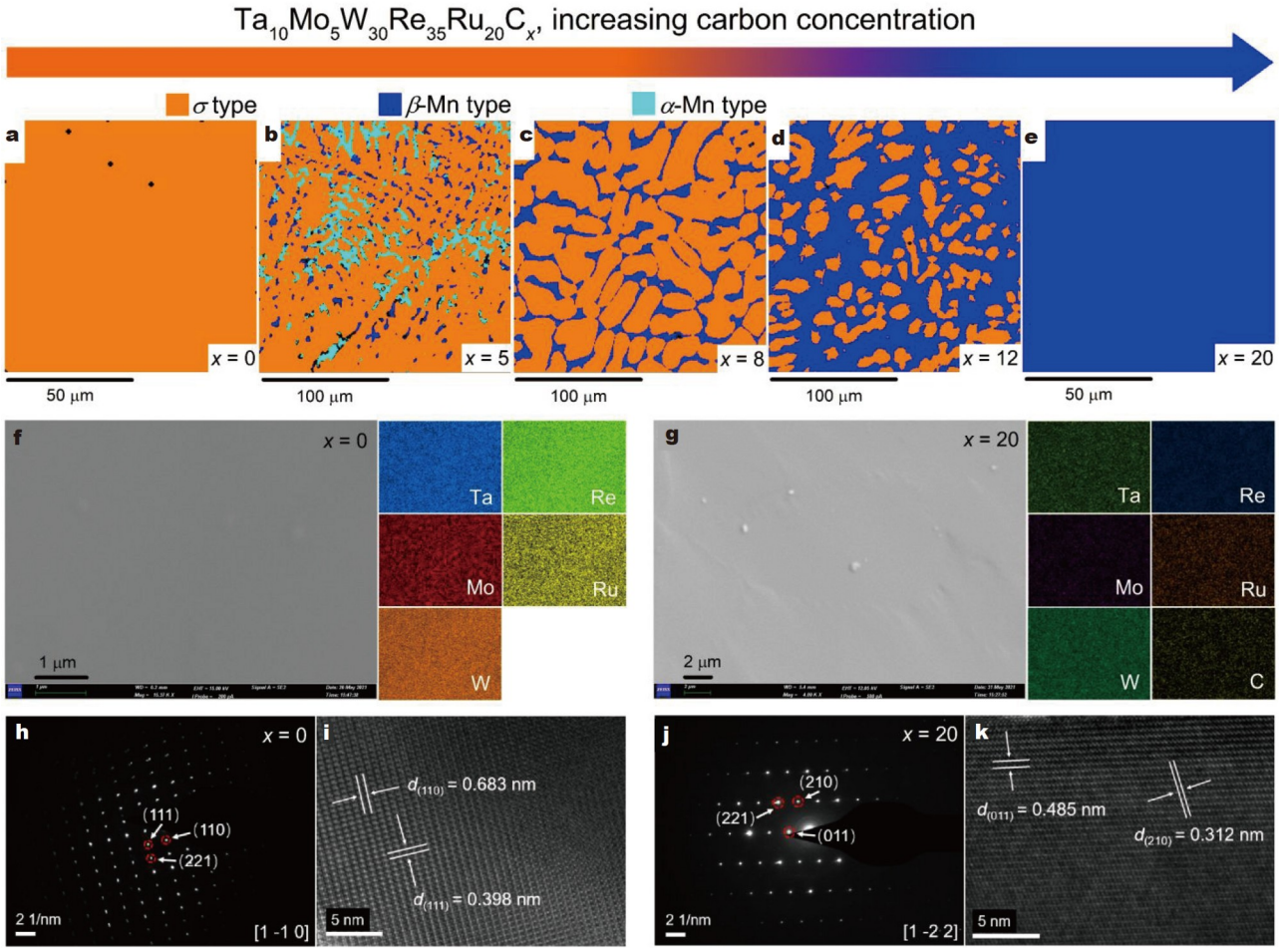

Figure 2 (a–e) EBSD phase maps for the $Ta_{10}Mo_5W_{30}Re_{35}Ru_{20}C_x$ HEAs with x = 0, 5, 8, 12 and 20, respectively. The arrow marks the direction of increasing carbon content. (f, g) SEM images together with EDX elemental mapping results for the HEAs with x = 0 and 20, respectively. (h, i) SAED pattern and the corresponding HRTEM image, respectively, taken along the [1 −1 0] zone axis of a single-crystalline grain for the σ type $Ta_{10}Mo_5W_{30}Re_{35}Ru_{20}C_x$ HEA (x = 0). (j, k) The same set of data taken along the [1 −2 2] zone axis of a single-crystalline grain for the β-Mn type $Ta_{10}Mo_5W_{30}Re_{35}Ru_{20}C_{20}$ HEA.

In the β-Mn type structure, however, there are only three different sites of 8*c* (0.0632, 0.0632, 0.0632), 12*d* (0.125, 0.2028, 0.4528) and 4*a* (0.375, 0.375, 0.375). The 8*c* and 12*d* sites are shared by all transition metal atoms, while the carbon atoms occupy the 4*a* one. As can be seen, the XRD pattern of x = 0 and 20 can be well fitted by a single σ (R_{wp} = 6.38%, R_p = 4.68%) and β-Mn type (R_{wp} = 10.99%, R_p = 7.88%) structure, respectively. As for x = 5, both σ and β-Mn type phases together with an α-Mn type ones are needed to achieve a good agreement between the calculated and observed XRD patterns (R_{wp} = 4.87%, R_p = 3.67%). It is worth noting that, in the β-Mn type structure, carbon is actually located at the interstitial position surrounded by six equivalent transition metal atoms, as expected from its small atomic radius.

Fig. 2a–e show the phase maps from EBSD measurements for the $Ta_{10}Mo_5W_{30}Re_{35}Ru_{20}C_x$ HEAs with x = 0, 5, 8, 12 and 20, respectively. Here the σ phase is shown in orange, β-Mn type phase shown in blue and α-Mn type phase shown in cyan. It is obvious that the C-free HEA (x = 0) has nearly 100% σ phase, which is gradually suppressed as the carbon content increases. Indeed, the HEA with x = 5 contains 83.4% σ phase, 8.9% α-Mn type phase and 5.1% β-Mn type phase. At a slightly higher x = 8, the α-Mn type phase is no longer detectable and the volume fraction of β-Mn type phase is increased to 18.2%. On further increasing x, the β-Mn type phase becomes dominant (64.5%) at x = 12, and finally a single β-Mn type phase is observed at x = 20.

These results are in good agreement with those from the XRD measurements and corroborate the occurrence of structural transformation due to carbon addition.

The single-phase $Ta_{10}Mo_5W_{30}Re_{35}Ru_{20}C_x$ HEAs with $x = 0$ and 20 are also characterized by SEM and TEM measurements. Typical SEM images together with EDX elemental mapping results are displayed in Fig. 2f, g. Both HEAs appear to be dense with a rather uniform distribution of the constituent elements. The measured Ta:Mo:W:Re:Ru = 9.5(1):4.3(1):30.2(1):35.3(1):20.7(1) for $x = 0$ and 9.6(1):4.6(1):29.8(1):35.2(1):20.8(1) for $x = 20$, in agreement with the nominal ratio. Since carbon has a light mass and is a mostly likely contaminant in the EDX analysis, its content cannot be determined accurately by the EDX measurements. Nevertheless, the actual carbon content should be close to nominal one given the negligible weight loss during the arc melting process. Fig. 2h–k show the selected-area electron diffraction (SAED) patterns and high-resolution TEM (HRTEM) images for these two HEAs. For $x = 0$, a well-defined SAED pattern is found along the [1 −1 0] zone axis of a single-crystalline grain, and the spots near the center are indexable to (110), (111), and (221) reflections of the σ type structure. Accordingly, the HRTEM image of the same grain reveals two lattice spacings of 0.683 and 0.398 nm, which match well with the (110) and (111) planes, respectively. On the other hand, the spots near the center of the SAED pattern for $x = 20$, which is taken along the [1 −2 2] zone axis of a single-crystalline grain, can be indexed to (011), (210), and (221) reflections of the β-Mn type structure. The corresponding HRTEM image gives two lattice spacings of 0.485 and 0.312 nm (Fig. 2k), which correspond well to the (011) and (210) planes. Therefore, both the pristine and transformed HEAs are homogeneous and possess a highly crystalline nature. Actually, we have also performed the EDX elemental mapping measurements for the HEAs with $x = 5$, 8 and 12. The results, which are provided in the Supplementary information (Figs S1–S3), reveal a uniform distribution of the carbon. Nevertheless, this should be taken with caution considering possible carbon contamination on the sample surface. On the other hand, the segregation of Re and Ru is clearly visible for $x = 5$ and 8, indicating that the α-Mn and β-Mn type phases (darker regions) contain less Re and more Ru than the σ one (lighter regions).

In addition to structural transformation, superconductivity is also observed in the $Ta_{10}Mo_5W_{30}Re_{35}Ru_{20}C_x$ HEAs. Since T_c is almost independent on x for both σ type and β-Mn type HEAs (see the insets of Fig. 3a, e), only those with $x = 0$ and 20 are characterized in detail and the results are displayed in Fig. 3a–h. In both cases, a resistivity drop, a large shielding fraction (>100%) and a distinct specific heat (C_p) jump are detected, providing evidence for a bulk superconducting transition. From the midpoint of resistivity drop, T_c is determined to be 4.87 and 5.34 K for $x = 0$ and 20, respectively. In the normal state, the C_p data can be well fitted by the equation

$$C_p / T = \gamma + \delta T^2 + \eta T^4, \quad (1)$$

where γ and $\delta(\eta)$ are the electronic and phonon specific heat coefficients, respectively. Then the Debye temperature Θ_D is calculated through

$$\Theta_D = (12\pi^4 R / 5\delta)^{1/3}, \quad (2)$$

where $R = 8.314$ J mol^{-1} K^{-1} is the molar gas constant. Thus, one obtains γ = 3.32 mJ molatom^{-1} K^{-2}, δ = 0.030 mJ molatom^{-1} K^{-4}, Θ_D = 381 K, and γ = 2.83 mJ molatom^{-1} K^{-2}, δ = 0.045 mJ molatom^{-1} K^{-4}, Θ_D = 342 K for $x = 0$ and 20, respectively. Once Θ_D is known, the

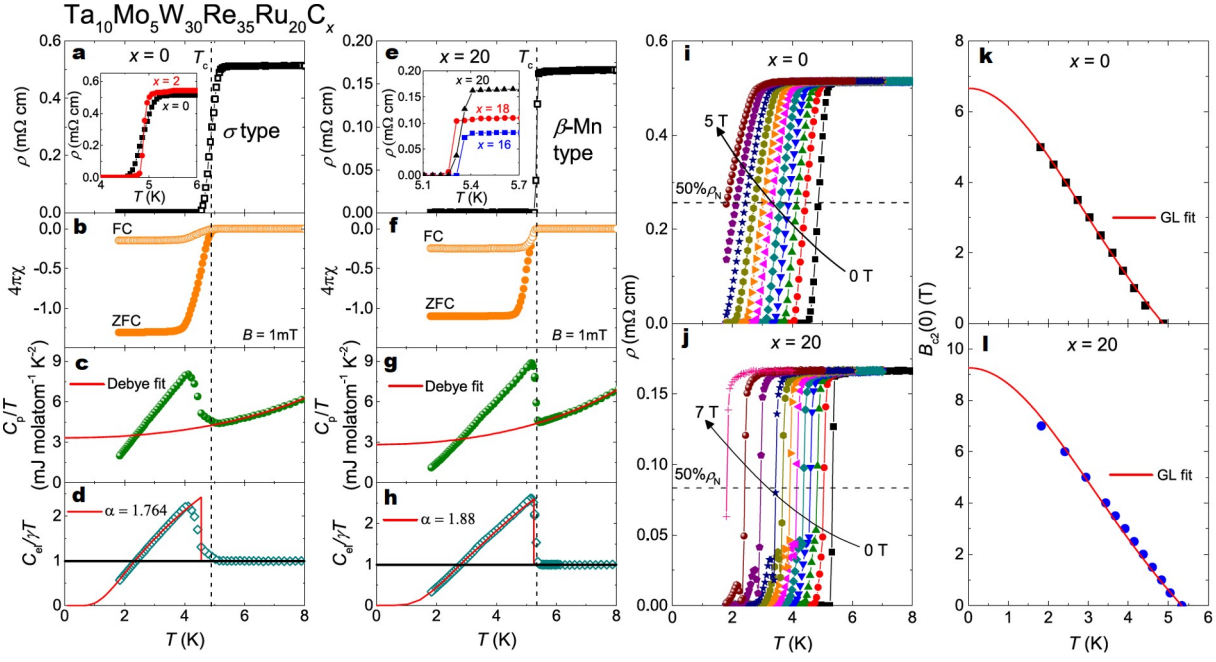

Figure 3 (a–d) Low temperature resistivity, susceptibility, specific heat, and normalized electronic specific heat data, respectively, for the σ type HEA with $x = 0$. In panel (a), the inset shows a comparison between the results for $x = 0$ and 2. In panels (c) and (d), the solid lines are fits to the data by the Debye model and α-model, respectively. (e–h) Same set of data for the β-Mn type HEA with $x = 20$. In panel (e), the inset shows a comparison between the results for $x = 16$, 18 and 20. In panels (g) and (h), the solid lines are fits to the data by the Debye model and α-model, respectively. (i, j) Temperature dependence of resistivity under various magnetic fields for the HEAs with $x = 0$ and 20, respectively. In both panels, the horizontal line denotes 50% drop of the normal-state resistivity. (k, l) Temperature dependence of the upper critical field for the two HEAs. In both panels, the solid line is a fit to the data by the GL model.

electron-phonon coupling strength λ_{ep} is estimated to be 0.59 for x = 0 and 0.62 for x = 20 on the basis of the inverted McMillan formula [37],

$$\lambda_{ep} = \frac{1.04 + \mu^* \ln(\Theta_D / 1.45T_c)}{(1 - 0.62\mu^*)\ln(\Theta_D / 1.45T_c) - 1.04}, \quad (3)$$

where μ^* = 0.13 is the Coulomb repulsion pseudopotential. By subtraction of the phonon contribution, the electronic specific heat C_{el} is isolated and plotted as $C_{el}/\gamma T$ *versus* T in Fig. 3d, h. The $C_{el}/\gamma T$ jumps of both HEAs can be well reproduced by the α-model, which was adapted from the single-band Bardeen-Cooper-Schrieffer (BCS) theory [38]. This model still assumes a fully isotropic superconducting gap but allows for the variation of coupling constant $\alpha = \Delta(0)/k_B T_c$, where $\Delta(0)$ is the gap size at 0 K. The resulting α = 1.764 for x = 0, which is exactly the value predicted by the BCS theory [39]. As for x = 20, a slightly larger α = 1.88 is obtained. These α values are consistent with magnitude of λ_{ep}, which together suggest that both σ type and β-Mn type HEAs have a weakly coupled, fully gapped superconducting state.

To determine the upper critical field B_{c2}, the temperature dependence of resistivity was measured under magnetic fields up to 7 T for the $Ta_{10}Mo_5W_{30}Re_{35}Ru_{20}C_x$ HEAs (x = 0 and 20), the results of which are displayed in Fig. 3i, j. As expected, the resistive transition is suppressed to lower temperatures as the field increases. Notably, for the HEA with x = 20, a resistivity tail appears in the field interval between 2 and 6 T. This seems to be a common feature for several β-Mn type superconductors [40,41] and is attributed to the weak links between the superconducting grains originating from the poor conducting grain boundaries. At each field, T_c is determined by the midpoint of ρ drop, and the constructed B_{c2} *versus* T phase diagrams are shown in Fig. 3k, l. The zero-temperature upper critical field $B_{c2}(0)$ is obtained by extrapolating the $B_{c2}(T)$ data based on the Ginzburg-Landau (GL) model

$$B_{c2}(T) = B_{c2}(0)\frac{1 - t^2}{1 + t^2}, \quad (4)$$

where $t = T/T_c$ is the reduced temperature. This gives $B_{c2}(0)$ = 6.7 and 9.3 T for x = 0 and 20, respectively. In particular, the latter value is comparable to the Pauli paramagnetic limit $B_P(0) = 1.86T_c \approx 9.9$ T [42]. With $B_{c2}(0)$, the GL coherence length $\xi_{GL}(0)$ is calculated to be 7.0 and 6.0 nm for x = 0 and 20, respectively, through the equation

$$\xi_{GL}(0) = \sqrt{\frac{\Phi_0}{2\pi B_{c2}(0)}}, \quad (5)$$

where $\Phi_0 = 2.07 \times 10^{-15}$ Wb is the flux quantum. All these parameters are summarized in Table 2.

It is known that the stability of HEAs is related to a few parameters [18,43,44], including valence electron concentration (VEC), atomic size difference (δ) and mixing entropy (ΔS_{mix}). Fig. 4a shows the VEC dependence of T_c for the σ type and β-Mn type $Ta_{10}Mo_5W_{30}Re_{35}Ru_{20}C_x$ HEAs, together with related HEA superconductors for comparison [11,32]. Here VEC is defined as

$$\mathrm{VEC} = \sum_{i=1}^{n} c_i (\mathrm{VEC})_i, \quad (6)$$

where c_i and $(\mathrm{VEC})_i$ are the molar fraction and number of valence electrons for the ith element, respectively. The VEC values of $Ta_{10}Mo_5W_{30}Re_{35}Ru_{20}C_x$ HEA superconductors are all located around 6.5, suggesting that they still obey the Matthias rule [45]. Specifically, T_c of the σ type HEAs ($0 \le x \le 2$) increases with increasing VEC from 6.60 to 6.65, which matches well with the trend reported previously [11]. In comparison, the VEC of β-Mn type HEAs ($16 \le x \le 20$) lies in a lower range of 6.21 to 6.28, and it has nearly no influence on T_c. This overall behavior, which is reminiscent of that observed in carbon added $(MoReRu)_{(1-2x)/3}(PdPt)_x$ HEAs [32], suggests that the decrease in VEC is key in driving the structural transformation. In passing, it is pointed out that the β-Mn type $Ta_{10}Mo_5W_{30}Re_{35}Ru_{20}C_x$ series are the first HEAs of this structure and have a considerably higher T_c than the fcc type $(MoReRu)_{(1-2x)/3}(PdPt)_xC_y$ ones.

We then compare the δ and ΔS_{mix} between the σ type and β-Mn type $Ta_{10}Mo_5W_{30}Re_{35}Ru_{20}C_x$ HEAs. For the σ type HEAs, the parameters are calculated according to the equations,

$$\delta = \sqrt{\sum_{i=1}^{n} c_i \left(1 - r_i / \sum_{i=1}^{n} c_i r_i\right)^2} \quad (7)$$

and

$$\Delta S_{mix} = -R \sum_{i=1}^{n} c_i \ln c_i, \quad (8)$$

where r_i is the atomic radius for the ith element. Regarding the β-Mn type HEAs, given the interstitial position of carbon, the total mixing entropy is the sum of metal and carbon sublattices, which is expressed as [46,47]

$$\Delta S_{mix} = \Delta S_{mix}^{metal} + \Delta S_{mix}^{carbon}. \quad (9)$$

The calculation results are plotted as a function of VEC in Fig. 4b, c. As can be seen, the δ is 2.18% and 6.58% for the σ type HEAs with x = 0 and 2, respectively, both of which are below the threshold value of ~6.6% for the formation of single phase HEAs [18]. In contrast, the δ values of the β-Mn type HEAs are considerably larger and range from 16.43% to 17.98%, meaning that the lattice distortion is significantly enhanced upon carbon addition. On the other hand, ΔS_{mix} is the same of 1.43R for the σ type HEA with x = 0 and the β-Mn type HEA with x = 20. Nevertheless, ΔS_{mix} is increased to 1.93R and 1.76R for the β-Mn type HEA with x = 16 and 18, respectively. Taken together, it is reasonable to speculate that the lattice distortion and mixing

Table 2 Structural refinement results and physical parameters of $Ta_{10}Mo_5W_{30}Re_{35}Ru_{20}C_x$ HEAs with x = 0 and 20

Parameter	x = 0	x = 20
Space group	$P4_2/mnm$	$P4_132$
a (Å)	9.6051(3)	6.8308(1)
c (Å)	4.9871(1)	–
V (Å^3)	460.11(2)	318.73(1)
R_{wp}	6.38%	10.99%
R_p	4.68%	7.88%
Goodness-of-fit (GOF)	1.69	1.88
T_c (K)	4.87	5.34
γ (mJ molatom^{-1} K^{-2})	3.32	2.83
δ (mJ molatom^{-1} K^{-4})	0.035	0.049
Θ_D (K)	381	342
λ_{ep}	0.59	0.63
$B_{c2}(0)$ (T)	6.7	9.3
$\xi_{GL}(0)$ (nm)	7.0	6.0

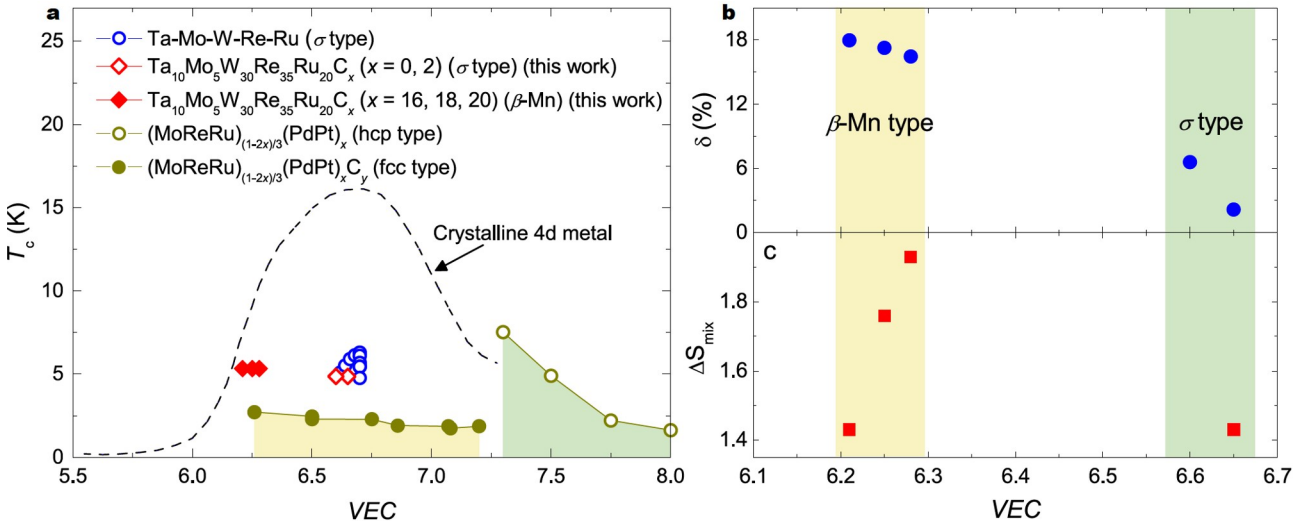

Figure 4 (a) VEC dependence of T_c for the σ type and β-Mn type $Ta_{10}Mo_5W_{30}Re_{35}Ru_{20}C_x$ HEAs, together with related systems for comparison. The dashed line denotes the behavior for crystalline 4d metals [45]. (b, c) Comparison between the VEC dependence of δ and ΔS_{mix}, respectively, for the two types of HEAs.

entropy also play a nontrivial role in the structural transformation of $Ta_{10}Mo_5W_{30}Re_{35}Ru_{20}C_x$.

Finally, we briefly discuss the implications of our results on future research. First, our results suggest that the structural transformation by adding carbon in HEAs may be a general consequence due to the decrease in VEC as well as the increase in lattice distortion and mixing entropy, which certainly calls for theoretical understandings. Second, our study points to a connection between the σ type and β-Mn type structures. In this regard, it is of interest to see whether β-Mn type phase could be obtained by carbon addition in binary and ternary σ type phases. Third, the lack of inversion symmetry in the β-Mn type $Ta_{10}Mo_5W_{30}Re_{35}Ru_{20}C_x$ HEAs may allow for a mixture of spin-singlet and spin-triplet pairing. Hence Muon spin rotation studies are worth pursuing to search for the signature of time-reversal symmetry breaking in the superconducting state.

CONCLUSIONS

In summary, we have studied the effect of carbon addition on the structure and physical properties of the $Ta_{10}Mo_5W_{30}Re_{35}Ru_{20}$ HEA. The results show that the $Ta_{10}Mo_5W_{30}Re_{35}Ru_{20}C_x$ HEA adopts a centrosymmetric tetragonal σ type structure for $0 \le x \le 2$, which transforms into a noncentrosymmetric cubic β-Mn type structure for $16 \le x \le 20$. Both the σ type and β-Mn type HEAs exhibit bulk superconductivity with T_c values of 4.87 and 5.34 K. Especially, the upper critical field of the latter reaches 9.3 T, which is close to the Pauli paramagnetic limit. A comparison of phase stability between the σ type and β-Mn type HEAs suggests that the decrease in VEC and the increase in lattice distortion and mixing entropy are mainly responsible for the structural transformation. Our study not only provides a rare example of centrosymmetric to noncentrosymmetric structural transformation in HEAs, but also consolidates that carbon addition is an efficient way to tune the structure and physical properties of HEAs.

Received 27 April 2022; accepted 31 May 2022;
published online 12 August 2022

1 Yeh JW, Chen SK, Lin SJ, *et al.* Nanostructured high-entropy alloys with multiple principal elements: Novel alloy design concepts and outcomes. Adv Eng Mater, 2004, 6: 299–303
2 Ye YF, Wang Q, Lu J, *et al.* High-entropy alloy: Challenges and prospects. Mater Today, 2016, 19: 349–362
3 Miracle DB, Senkov ON. A critical review of high entropy alloys and related concepts. Acta Mater, 2017, 122: 448–511
4 Zhang W, Liaw PK, Zhang Y. Science and technology in high-entropy alloys. Sci China Mater, 2018, 61: 2–22
5 George EP, Raabe D, Ritchie RO. High-entropy alloys. Nat Rev Mater, 2019, 4: 515–534
6 Li W, Xie D, Li D, *et al.* Mechanical behavior of high-entropy alloys. Prog Mater Sci, 2021, 118: 100777
7 Wang X, Guo W, Fu Y. High-entropy alloys: Emerging materials for advanced functional applications. J Mater Chem A, 2021, 9: 663–701
8 Stolze K, Tao J, von Rohr FO, *et al.* Sc-Zr-Nb-Rh-Pd and Sc-Zr-Nb-Ta-Rh-Pd high-entropy alloy superconductors on a CsCl-type lattice. Chem Mater, 2018, 30: 906–914
9 Stolze K, Cevallos FA, Kong T, *et al.* High-entropy alloy superconductors on an α-Mn lattice. J Mater Chem C, 2018, 6: 10441–10449
10 Liu B, Wu J, Cui Y, *et al.* Structural evolution and superconductivity tuned by valence electron concentration in the Nb-Mo-Re-Ru-Rh high-entropy alloys. J Mater Sci Tech, 2021, 85: 11–17
11 Liu B, Wu JF, Cui Y, *et al.* Formation and superconductivity of single-phase high-entropy alloys with a tetragonal structure. ACS Appl Electron Mater, 2020, 2: 1130–1137
12 Liu B, Wu J, Cui Y, *et al.* Superconductivity and paramagnetism in Cr-containing tetragonal high-entropy alloys. J Alloys Compd, 2021, 869: 159293
13 Wu J, Liu B, Cui Y, *et al.* Polymorphism and superconductivity in the V-Nb-Mo-Al-Ga high-entropy alloys. Sci China Mater, 2020, 63: 823–831
14 Yamashita A, Matsuda TD, Mizuguchi Y. Synthesis of new high-entropy alloy-type Nb_3(Al,Sn,Ge,Ga,Si) superconductors. J Alloys Compd, 2021, 868: 159233
15 Lee C, Chou Y, Kim G, *et al.* Lattice-distortion-enhanced yield strength in a refractory high-entropy alloy. Adv Mater, 2020, 32: 2004029
16 An Z, Mao S, Liu Y, *et al.* A novel HfNbTaTiV high-entropy alloy of superior mechanical properties designed on the principle of maximum lattice distortion. J Mater Sci Tech, 2021, 79: 109–117
17 Tang Z, Huang L, He W, *et al.* Alloying and processing effects on the aqueous corrosion behavior of high-entropy alloys. Entropy, 2014, 16: 895–911
18 Zhang Y, Zuo TT, Tang Z, *et al.* Microstructures and properties of high-entropy alloys. Prog Mater Sci, 2014, 61: 1–93

19 Shi Y, Yang B, Xie X, *et al.* Corrosion of $Al_xCoCrFeNi$ high-entropy alloys: Al-content and potential scan-rate dependent pitting behavior. Corrosion Sci, 2017, 119: 33–45
20 Hua N, Wang W, Wang Q, *et al.* Mechanical, corrosion, and wear properties of biomedical Ti-Zr-Nb-Ta-Mo high entropy alloys. J Alloys Compd, 2021, 861: 157997
21 Vaidya M, Guruvidyathri K, Murty BS. Phase formation and thermal stability of CoCrFeNi and CoCrFeMnNi equiatomic high entropy alloys. J Alloys Compd, 2019, 774: 856–864
22 Whitfield TE, Pickering EJ, Owen LR, *et al.* An assessment of the thermal stability of refractory high entropy superalloys. J Alloys Compd, 2021, 857: 157583
23 von Rohr F, Winiarski MJ, Tao J, *et al.* Effect of electron count and chemical complexity in the Ta-Nb-Hf-Zr-Ti high-entropy alloy superconductor. Proc Natl Acad Sci USA, 2016, 113: E7144–E7150
24 Guo J, Wang H, von Rohr F, *et al.* Robust zero resistance in a superconducting high-entropy alloy at pressures up to 190 GPa. Proc Natl Acad Sci USA, 2017, 114: 13144–13147
25 Wang Z, Baker I, Cai Z, *et al.* The effect of interstitial carbon on the mechanical properties and dislocation substructure evolution in $Fe_{40.4}Ni_{11.3}Mn_{34.8}Al_{7.5}Cr_6$ high entropy alloys. Acta Mater, 2016, 120: 228–239
26 Wang Z, Baker I. Interstitial strengthening of a f.c.c. FeNiMnAlCr high entropy alloy. Mater Lett, 2016, 180: 153–156
27 Li Z, Tasan CC, Springer H, *et al.* Interstitial atoms enable joint twinning and transformation induced plasticity in strong and ductile high-entropy alloys. Sci Rep, 2017, 7: 40704
28 Chen LB, Wei R, Tang K, *et al.* Heavy carbon alloyed FCC-structured high entropy alloy with excellent combination of strength and ductility. Mater Sci Eng-A, 2018, 716: 150–156
29 Zhang C, Bhandari U, Zeng C, *et al.* Carbide formation in refractory $Mo_{15}Nb_{20}Re_{15}Ta_{30}W_{20}$ alloy under a combined high-pressure and high-temperature condition. Entropy, 2020, 22: 718
30 Casillas-Trujillo L, Jansson U, Sahlberg M, *et al.* Interstitial carbon in bcc HfNbTiVZr high-entropy alloy from first principles. Phys Rev Mater, 2020, 4: 123601
31 Cui Y, Zhu Q, Xiao G, *et al.* Interstitially carbon-alloyed refractory high-entropy alloys with a body-centered cubic structure. Sci China Mater, 2022, 65: 494–500
32 Zhu Q, Xiao G, Cui Y, *et al.* Structural transformation and superconductivity in carbon-added hexagonal high-entropy alloys. J Alloys Compd, 2022, 909: 164700
33 Hall EO, Algie SH. The sigma phase. Int Mater Rev, 1966, 11: 61–88
34 Tsai MH, Tsai KY, Tsai CW, *et al.* Criterion for sigma phase formation in Cr- and V-containing high-entropy alloys. Mater Res Lett, 2013, 1: 207–212
35 Tsai MH, Chang KC, Li JH, *et al.* A second criterion for sigma phase formation in high-entropy alloys. Mater Res Lett, 2016, 4: 90–95
36 Petříček V, Dušek M, Palatinus L. Crystallographic computing system JANA2006: General features. Z für Kristallographie-Crystline Mater, 2014, 229: 345–352
37 McMillan WL. Transition temperature of strong-coupled superconductors. Phys Rev, 1968, 167: 331–344
38 Johnston DC. Elaboration of the α-model derived from the BCS theory of superconductivity. Supercond Sci Technol, 2013, 26: 115011
39 Bardeen J, Cooper LN, Schrieffer JR. Theory of superconductivity. Phys Rev, 1957, 108: 1175–1204
40 Kawashima K, Kawano A, Muranaka T, *et al.* Superconductivity in intermetallic $W_7Re_{13}X$ (X = B and C) compounds. J Phys Soc Jpn, 2005, 74: 700–704
41 Zhu Q, Xiao G, Cui Y, *et al.* W_4IrC_{1-x}: A new noncentrosymmetric superconductor with a cubic β-Mn type structure. J Mater Chem C, 2022, 10: 6070–6077
42 Clogston AM. Upper limit for the critical field in hard superconductors. Phys Rev Lett, 1962, 9: 266–267
43 Zhang Y, Zhou Y , Lin J , *et al.* Solid-solution phase formation rules for multi-component alloys. Adv Eng Mater, 2008, 10: 534–538
44 Guo S, Ng C, Lu J, *et al.* Effect of valence electron concentration on stability of fcc or bcc phase in high entropy alloys. J Appl Phys, 2011, 109: 103505
45 Matthias BT. Empirical relation between superconductivity and the number of valence electrons per atom. Phys Rev, 1955, 97: 74–76
46 Rogal L, Bobrowski P, Körmann F, *et al.* Computationally-driven engineering of sublattice ordering in a hexagonal AlHfScTiZr high entropy alloy. Sci Rep, 2017, 7: 2209
47 Zhang P, Liu X, Cai A, *et al.* High-entropy carbide-nitrides with enhanced toughness and sinterability. Sci China Mater, 2021, 64: 2037–2044

Acknowledgements We thank the financial support by the foundation of Westlake University and the Service Center for Physical Sciences for technical assistance in SEM measurements. The work at Zhejiang University is supported by the National Natural Science Foundation of China (12050003).

Author contributions Xiao G initialized the project, synthesized the samples and did the physical property measurements with the assistance from Zhu Q, Yang W, Cui Y, Song S and Cao GH. Ren Z supervised the project and wrote the paper with input from Xiao G.

Conflict of interest The authors declare that they have no conflict of interest.

Supplementary information Supporting data are available in the online version of the paper.

Guorui Xiao is currently a PhD student at the School of Science, Westlake University. He received his bachelor degree from Taiyuan University of Technology in 2013, and Master degree from Guangxi University in 2018. His research interests include the exploration and characterization of novel superconductors and functional materials.

Zhi Ren has been a principle investigator at the School of Science, Westlake University since 2017. He received his bachelor and doctoral degrees from Zhejiang University in 2004 and 2009, respectively. He was a specially appointed researcher at Osaka University from 2009 to 2012 and a postdoctoral assistant at the University of Geneva from 2013 to 2017. His research interests include the superconductivity and topological quantum state of materials.

碳添加引起一种超导高熵合金的中心对称到非中心对称结构转变

肖国锐[1,2,3], 祝钦清[1,2,4], 杨武璋[1,2,4], 崔艳威[1,2,3], 宋世杰[3], 曹光旱[3], 任之[1,2*]

摘要 四方σ相是过渡金属合金中最常见的物相之一. 然而, σ型高熵合金中尚未有关于碳添加效应的报道. 在本文中, 我们发现在超导的$Ta_{10}Mo_5W_{30}Re_{35}Ru_{20}$高熵合金($T_c$ = 4.87 K)中添加碳会引起结构转变. 结果表明在$0 \le x \le 2$时$Ta_{10}Mo_5W_{30}Re_{35}Ru_{20}C_x$高熵合金具有中心对称的σ型结构, 但在$16 \le x \le 20$时转变为非中心对称的β-Mn型结构. 转变后的β-Mn型高熵合金仍表现出体超导电性且具有更高的T_c (5.34 K)和接近泡利顺磁极限的上临界场. 此外, 该结构转变归因于碳添加引起价电子浓度的降低以及晶格畸变和混合熵的增加. 我们的研究结果不仅提供了高熵合金中中心对称到非中心对称结构转变的罕见例子, 而且夯实了非金属碳是调节高熵合金结构和物理性质的有效添加剂.

